# A HIERARCHICAL MULTISCALE METHOD FOR TWO-PHASE FLOW BASED UPON MIXED FINITE ELEMENTS AND NONUNIFORM COARSE GRIDS

JØRG E. AARNES, STEIN KROGSTAD & KNUT–ANDREAS LIE*

**Abstract.** We analyse and further develop a hierarchical multiscale method for the numerical simulation of two-phase flow in highly heterogeneous porous media. The method is based upon a mixed finite-element formulation, where fine-scale features are incorporated into a set of coarse-grid basis functions for the flow velocities. By using the multiscale basis functions, we can retain the efficiency of an upscaling method by solving the pressure equation on a (moderate-sized) coarse grid, while at the same time produce a detailed and conservative velocity field on the underlying fine grid.

Earlier work has shown that the multiscale method performs excellently on highly heterogeneous cases using uniform coarse grids. In this paper, we extend the methodology to nonuniform and unstructured coarse grids and discuss various formulations for generating the coarse-grid basis functions. Moreover, we focus on the impact of large-scale features such as barriers or high-permeable channels and discuss potentially problematic flow cases. To improve the accuracy of the multiscale solution, we introduce adaptive strategies for the coarse grids, based on either local hierarchical refinement or on adapting the coarse grid more directly to large-scale permeability structures of arbitrary shape. The resulting method is very flexible with respect to the size and the geometry of coarse-grid cells, meaning that grid refinement/adaptation can be performed in a straightforward manner. The suggested strategies are illustrated in several numerical experiments.

**Key words.** multiscale finite element methods, two-phase flow, porous media, reservoar simulation, non-uniform grids

**1. Introduction.** Flow in porous rock formations occurs on a wide span of length scales, from the micrometre scale of short and narrow pore channels to, for instance, the size of huge oil and groundwater reservoirs possibly stretching across several tens of kilometres. Petroleum reservoirs, for instance, are often created by a series of geological processes and may contain rock types with very different abilities to transmit fluid flow. The permeability (conductivity) of the porous rock formations may therefore span several orders of magnitude, from nearly impermeable barriers to high-permeable flow channels. In addition, fractures and faults may penetrate the entire reservoir in the vertical direction, causing sharp transition zones. Finally, in fluvial reservoirs the predominant flow may follow intertwined flow channels that form a highly irregular pattern. It is obvious that with this type of complexity, one cannot hope to model all pertinent scales that impact flow in heterogeneous porous media. Instead it is customary to create models for studying phenomena occurring at a specific length scale, or at a limited range of length scales only. This, however, cannot be done rigorously without also linking the particular model to appropriate subscale and large-scale flow models, i.e., taking the multiscale nature of the problem into account.

Multiscale problems pose a continuing challenge to mathematical modelling and simulation, and many different techniques have been proposed. The use of upscaling, i.e., the design of 'coarse' grid models by using some kind of averaging procedure to derive suitable parameterisations of the relevant geophysical quantities such as porosity and permeability, is widespread in both reservoir simulation and groundwater hydrology, see e.g., [8, 11, 12, 26, 27]. The motivation behind this approach is to get a quantitative picture of the general flow behaviour at the coarse scale. Available

*SINTEF ICT, Applied Mathematics, P.O. Box 124 Blindern, N–0314 Oslo, Norway. The research was funded by the Research Council of Norway under grants no. 158908/I30 and 162606/V30.

information about the fine-scale heterogeneous structures is therefore discarded once the upscaling has been performed. Thus, in standard flow modelling using upscaling, it is in general not possible to recover fine-scale flow patterns from the upscaled solution on a coarse grid in a mathematically rigorous way. In other words, the fine-scale details are lost and one can at best hope to capture the large-scale features of the flow pattern.

In recent years, it has been recognised that it is important to incorporate inter-scale effects for many problems exhibiting a multiscale structure. That is, to correctly model a phenomenon at a given range of length scales, one often has to take into account effects from physical phenomena occurring also at length scales outside the primary range of interest. For instance, to model large-scale flow behaviour in a porous medium correctly it is necessary to simultaneously model small-scale flow patterns. This realisation has spurred the development of so-called multiscale methods, see e.g. [18, 19, 7, 4, 25, 15, 16, 10]. In these methods the impact of small-scale structures are incorporated into a set of coarse-scale equations in a way that is mathematically consistent with the local property of the differential operator. Moreover, many multiscale methods are designed so that it is easy to recover fine-scale details from the coarse-grid solution.

In this paper we consider a multiscale mixed finite-element method (MsMFEM) that has been applied successfully to simulate two-phase flows in strongly heterogeneous porous media [1, 2]. The method is a variant of the MsMFEM introduced by Chen and Hou in [10], and also closely related to the *subgrid upscaling* introduced by Arbogast [7, 4, 5]. The connection between these two approaches has recently been addressed in [6]. We also mention here work by Kuznetsov et al. [24, 23], where the focus is on mixed FEMs for general polygonal/polyhedral grids rather than on multiscale properties. In fact, the method suggested in [24, 23] is very similar to the method of Chen and Hou [10] (without oversampling) if the fine subgrid is taken as a triangular/tetrahedral sub-partitioning.

The main idea behind the MsMFEM is to model fine-scale patterns in the velocity field by computing special finite-element base functions that reflect the impact of the fine-scale heterogeneous structures. In this two-grid approach, the pressure equation is solved on a coarse grid using locally defined basis functions that are computed numerically by solving flow problems on an underlying fine grid. In other words, large scale effects are accounted for by the degrees of freedom on a coarse grid, and fine-scale effects are accounted for by subresolution in the basis functions. Using results from homogenisation theory (see e.g., [9, 17, 22]), Chen and Hou [10] were able to derive convergence estimates for problems with two-scale periodic coefficients. However, because this method is mass conservative on the fine scale only up to the treatment of wells, the fine-scale velocity field recovered from the coarse-scale solution cannot model fine-scale flow correctly. Aarnes [1] therefore proposed a modification of the method, where special care was taken to ensure a fine-scale conservative velocity field also in the coarse bocks containing wells. Hence, using this method for the elliptic pressure equation makes it possible to simulate fluid transport without employing time-consuming and potentially unreliable upscaling procedures for the fluid transport equations. We note that the subgrid upscaling approach [7, 4, 5] also produces a fully conservative fine-scale velocity field, and thus seems to be the first appearing related method fulfilling this property.

Durlofsky et al. [13] proposed an alternative approach to avoid upscaling the transport equation. Their idea was to employ nonuniformly coarsened grids with low

resolution in low-flow regions and high resolution in high-flow regions. Thus, instead of modelling subgrid effects explicitly, the authors proposed to minimise errors caused by disregarding subgrid effects by introducing higher grid resolution in regions where subgrid terms otherwise would be important. Here we borrow ideas from the nonuniform coarsening approach to improve the accuracy and robustness of the MsMFEM. Experience has shown that we may loose accuracy when large scale features penetrate a coarse grid block. However, this loss of accuracy does not necessarily occur in high-flow regions, but rather in regions of rapid change of flow due to, for instance, a barrier of very low permeability that transverses a coarse grid block. Hence, for the current purpose it is clear that we need to select different grid refinement criteria than the ones employed in [13].

The main objectives in this paper are: (*i*) extend the hierarchical multiscale method (MsMFEM) to nonuniform and unstructured coarse grids; (*ii*) identify in which situations the method suffers from loss of accuracy; (*iii*) select criteria that detect the problems; and (*iv*) propose efficient remedies based on nonuniform coarsening. We shall see that the MsMFEM is very flexible with respect to grid-block geometries and that this facilitates very general grid-refinement procedures, since we have few restrictions on the shape of the resulting grid blocks. However, one should keep in mind that the MsMFEM operates on two grids, and that refining the coarse grid need not necessarily improve the accuracy. The reason for this is that heterogeneities in the coefficients are accounted for in two different ways in the MsMFEM: fine-scale heterogeneities are incorporated in basis functions giving subgrid resolution, while large-scale flow-patterns are taken into account when solving the coarse-grid problems. Thus, in the decision of a suitable coarse grid, the scales may pull us in opposite directions; fine-scale features with short correlation length are best resolved in large coarse-grid blocks, while structures with long correlation lengths are often too large to be resolved in the basis functions and may be better resolved using small coarse-grid blocks. This illustrates that grid-refinement strategies for the multiscale method may be very different from strategies used for conventional (single-scale) method and that finding an *optimal* coarse grid may be nontrivial. On the other hand, the multiscale method is seldom very sensitive in practise to the choice of a coarse grid. Therefore, the combination of subscale resolution and flexibility and robustness with respect to the choice of a coarse grid makes the MsMFEM a highly versatile tool for flow simulations in strongly heterogeneous porous media.

The paper is organised as follows. In Section 2 we introduce the mathematical model for two phase incompressible flow. In Sections 3 and 4 we describe the multiscale mixed FEM and discuss relevant choices of approximation spaces. Griding strategies are presented in Section 5 and several numerical examples in Section 6.

**2. A Two-Phase Model for Incompressible Flow.** We consider a model for incompressible two-phase flow with no gravity or capillary pressure. The equations are derived from conservation of mass for each phase $j$:

$$\phi \frac{\partial S_j}{\partial t} + \nabla \cdot v_j = q_j, \tag{2.1}$$

where the phase velocities $v_j$ are given by Darcy's law:

$$v_j = -\lambda_j(S_j) K \nabla p_j. \tag{2.2}$$

Here $\phi$ is the porosity, $S_j$ is the saturation of phase $j$ (fraction of the void occupied by phase $j$), and $q_j$ is a source (or sink) term. In the Darcy equations, $K$ is the

permeability tensor, $p_j$ is the phase pressure, and $\lambda_j$ is the phase mobility given by $\lambda_j(S_j) = k_{rj}(S_j)/\mu_j$, where $k_{rj}$ and $\mu_j$ are the relative permeability and viscosity of phase $j$, respectively. The relative permeability models the reduced conductivity of a phase due to the presence of other phases, and is, according to common practise, assumed to be a function of the saturations only.

Let the two phases be oil and water ($j = o, w$). Since we neglect effects from capillary pressure so that $\nabla p_o = \nabla p_w$, we might as well assume $p_o = p_w = p$. Then the Darcy equations combined with conservation of mass yield the *pressure equation*:

$$v = -(\lambda_w + \lambda_o)K\nabla p, \qquad \nabla \cdot v = q, \tag{2.3}$$

where $v = v_w + v_o$ and $q = q_w + q_o$. We assume that the two phases occupy the void space completely and introduce the water *fractional flow* $f_w = \lambda_w/\lambda$, where $\lambda(S_w) = \lambda_w(S_w)+\lambda_o(1-S_w)$ is the total mobility. We may then write the conservation equation for water, henceforth called the *saturation equation*, as follows:

$$\phi\frac{\partial S_w}{\partial t} + \nabla \cdot (f_w v) = q_w. \tag{2.4}$$

In the following we will, for ease of notation, drop the subscripts of $S_w$ and $f_w$. As in [1], the system of equations (2.3)–(2.4) will be solved using a sequential splitting, where the pressure equation at each time step is solved with the MsMFEM using coefficients depending on saturation values from the previous time step, and the saturation equation is solved with an upstream-weighted finite-volume method (see Section 6).

**3. A Multiscale Method for the Pressure Equation.** The concept of a multiscale mixed finite-element method for solving second-order elliptic problems with coefficients spanning multiple scales was first introduced by Arbogast et al. [7], and in the formulation we use in this paper by Chen and Hou [10]. In the following (sub)sections we will review the MsMFEM of [1, 2, 3] and show how the method can be extended to nonuniform and unstructured coarse grids.

**3.1. Mixed Finite Elements.** Let $\Omega$ be a domain in $\mathbb{R}^d$, and denote by $\nu$ the outward-pointing unit normal on $\partial\Omega$. Consider now the pressure equation (2.3) in $\Omega$ with no-flow boundary conditions, i.e., $v \cdot \nu = 0$ on $\partial\Omega$. Note that in this case $p$ is defined only up to a multiplicative constant, so one needs an additional constraint such as $\int_\Omega p\,dx = 0$ to close the system. We introduce next the function space

$$H_0^{\mathrm{div}}(\Omega) = \left\{ v \in (L^2(\Omega))^d \ : \ \nabla \cdot v \in L^2(\Omega) \text{ and } v \cdot \nu = 0 \text{ on } \partial\Omega \right\}.$$

The current mixed FEM discretisation of the pressure equation seeks a pair $(v, p) \in U \times V$, where $U$ and $V$ are finite-dimensional subspaces of $H_0^{\mathrm{div}}(\Omega)$ and $L^2(\Omega)$, respectively, such that

$$\int_\Omega v \cdot (\lambda K)^{-1} u \, dx - \int_\Omega p \nabla \cdot u \, dx = 0, \qquad \text{for all } u \in U, \tag{3.1}$$

$$\int_\Omega l \nabla \cdot v \, dx = \int ql \, dx, \qquad \text{for all } l \in V. \tag{3.2}$$

Thus, letting $\{\psi_i\}$ and $\{\phi_k\}$ be bases for $U \subset H_0^{\mathrm{div}}(\Omega)$ and $V \subset L^2(\Omega)$, we obtain approximations $v = \sum v_i\psi_i$ and $p = \sum p_k\phi_k$, where the coefficients $\mathbf{v} = \{v_i\}$ and $\mathbf{p} = \{p_k\}$ solve the linear system

$$\begin{bmatrix} \mathbf{B} & \mathbf{C} \\ \mathbf{C}^T & \mathbf{O} \end{bmatrix} \begin{bmatrix} \mathbf{v} \\ -\mathbf{p} \end{bmatrix} = \begin{bmatrix} \mathbf{0} \\ \mathbf{q} \end{bmatrix}. \tag{3.3}$$

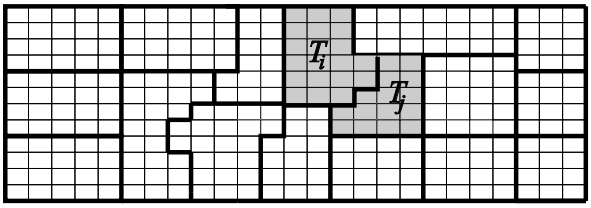


FIG. 3.1. *A general coarse grid overlying a uniform fine grid. The shaded region shows the support domain of basis function* $\psi_{ij}$.

Here $\mathbf{B} = \{b_{ij}\}$, $\mathbf{C} = \{c_{ik}\}$, and $\mathbf{q} = \{q_k\}$ are defined by

$$b_{ij} = \int_\Omega \psi_i \cdot (\lambda K)^{-1} \psi_j \, dx, \quad c_{ik} = \int_\Omega \phi_k \nabla \cdot \psi_i \, dx, \quad \text{and} \quad q_k = \int_\Omega \phi_k q \, dx.$$

In standard discretisation methods the spaces $U$ and $V$ typically consist of low-order piecewise polynomials. In multiscale methods, however, one requires that the basis functions should be adaptive to the local property of the differential operator. We will denote the approximation spaces for our MsMFEM by $U_{\text{ms}}$ and $V$. For incompressible flows the actual pressure solution is immaterial for the flow simulation, only the velocity field is needed. We will therefore construct a multiscale approximation space $U_{\text{ms}}$ for velocity only and use a standard approximation space $V$ for pressure as described in the next subsection. We return to a more thorough discussion of the approximation space $U_{\text{ms}}$ for velocity in Section 4.

**3.2. The MsMFEM Approximation Spaces.** The main focus of this paper is a completely local version of the MsMFEM (see [3]); that is, a multiscale method for which no *a priori* knowledge of the global flow pattern is assumed. This version is described next. In Section 3.2.2, we also describe the global approach from [1], where information from a global velocity field computed directly on the fine grid is incorporated into the basis functions.

Let $\mathcal{K} = \{K_m\}$ be a partitioning of $\Omega$ into mutually disjoint grid cells. Furthermore, let $\mathcal{T} = \{T_i\}$ be a coarser partitioning of $\Omega$, in such a way that whenever $K_m \cap T_i \neq 0$ then $K_m \subset T_i$. As an example, consider Figure 3.1. Here the *fine grid* $\mathcal{K}$ is uniform, while the *coarse grid* $\mathcal{T}$ has cells of more arbitrary shapes. Let $\Gamma_{ij}$ denote the non-degenerate interfaces $\Gamma_{ij} = \partial T_i \cap \partial T_j$. For each $\Gamma_{ij}$ we assign a basis function $\psi_{ij} \in U_{\text{ms}}$, and for each $T_i$ we assign a basis function $\phi_i \in V$.

**3.2.1. Local Basis Functions for Velocity.** In the local approach, a basis function $\psi_{ij}$ corresponding to an interface $\Gamma_{ij}$ is obtained by forcing a unit displacement from cell $T_i$ to $T_j$. That is, in the subdomain $\Omega_{ij} = T_i \cup \Gamma_{ij} \cup T_j$ we solve (approximately) a local flow problem of the form

$$\psi_{ij} = -\lambda K \nabla \phi_{ij}, \quad \nabla \cdot \psi_{ij} = \begin{cases} w_i(x), & \text{for } x \in T_i, \\ -w_j(x), & \text{for } x \in T_j, \end{cases} \tag{3.4}$$

with $\psi \cdot \nu = 0$ on $\partial\Omega_{ij}$, where $\nu$ is the outward-pointing unit normal to $\partial\Omega_{ij}$ pointing from $T_i$ to $T_j$. Here $w_i(x)$ is a *source distribution function* assigned to $T_i$. The source function is normalised such that $\int_{T_i} w_i = 1$. For cells containing a well, i.e., for all $T_i$

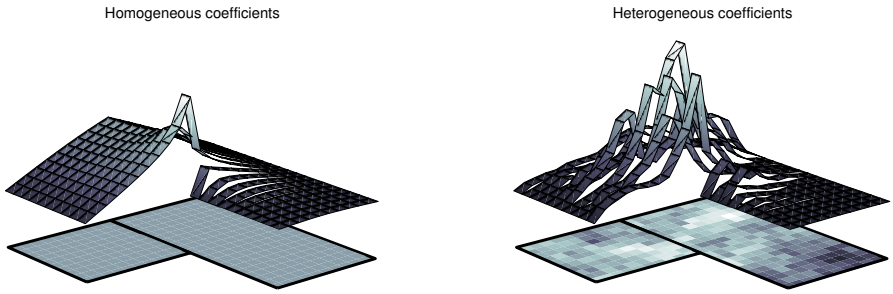


FIG. 3.2. *Velocity basis function associated with an edge between two cells of different size in 2D. The plots show the x-component in the case with homogeneous and heterogeneous coefficients, respectively.*

such that $\int_{T_i} q \neq 0$, we make a special choice of the weight function,

$$w_i(x) = \frac{q(x)}{\int_{T_i} q(\xi)\, d\xi}, \tag{3.5}$$

to ensure a conservative approximation on the fine grid (see Section 3.2.3). For cells with no source, the weight function $w_i(x)$ can, at least in principle, be chosen almost arbitrarily. A simple approach is to use a uniform source, i.e., choose $w_i(x) = 1/|T_i|$, which we will assume henceforth. In Section 4.1 we give a more thorough discussion of what are the appropriate choices for $w_i(x)$.

**3.2.2. Global Basis Functions for Velocity.** Assume now that a global fine-grid velocity field $v$ has been computed in advance, e.g., based on the initial saturation distribution. It might then be a good idea to exploit information from this solution in the construction of the velocity basis functions. Indeed, for basis functions with support domain $\Omega_{ij}$ as defined above, we know that $v_{\text{ms}}$ is determined solely by the behaviour of the base functions at the coarse-grid interfaces. In particular, if $\nu_{ij}$ is the unit normal to $\Gamma_{ij}$ pointing from $T_i$ to $T_j$ and

$$\psi_{ij} \cdot \nu_{ij}|_{\Gamma_{ij}} = \frac{(v \cdot \nu_{ij})|_{\Gamma_{ij}}}{\int_{\Gamma_{ij}} (v \cdot \nu_{ij})\, ds},$$

then $v_{\text{ms}} = v$ (see Section 3.2.3). Thus, we are able to replicate $v$ by imposing this type of boundary conditions at the coarse-grid interfaces. This means that, instead of solving only one local pressure equation in $\Omega_{ij}$ for each base function $\psi_{ij}$, we must solve one pressure equation in $T_i$ and one pressure equation in $T_j$ to compute the base function $\psi_{ij}$ associated with $\Gamma_{ij}$.

This approach is clearly not very useful if the pressure equation needs to be solved only once, but for multiphase flow simulations, where the pressure equation is solved repeatedly throughout the simulation, solving for $(p, v)$ once on a fine grid can be justified. To illustrate, let $v$ denote an initial fine-grid velocity field. To define a multiscale basis function $\psi_{ij}$ associated with $\Gamma_{ij}$ at time $t_n$, we may therefore use

(3.4) subject to the following boundary conditions

$$\psi_{ij} \cdot \nu_{ij} = 0 \quad \text{on } \partial\Omega_{ij}$$
$$\psi_{ij} \cdot \nu_{ij} = \frac{\mu_{ij}(x,t_n)}{\int_{\Gamma_{ij}} \mu_{ij}(s,t_n)ds}, \quad \mu_{ij}(x,t) = \frac{\lambda(x,t)}{\lambda(x,t_0)}(v(x)\cdot\nu_{ij}) \quad \text{on } \Gamma_{ij}.$$

In the global approach, the choice of source distribution $w_i(x)$ in cells without sources has no effect on $v_{\text{ms}}$, so we use simply $w_i = 1/|T_i|$. This option was considered in [1, 2].

**3.2.3. Basis Functions for Pressure.** To approximate the pressure we will use functions that are constant on each coarse grid block. Thus $V = \text{span}\,(\{\phi_i\})$, where

$$\phi_i(x) = \begin{cases} 1 & \text{if } x \in T_i, \\ 0 & \text{otherwise.} \end{cases} \tag{3.6}$$

This type of approximation space for pressure is also used in the lowest-order Raviart–Thomas method, and in the MsMFEM proposed by Chen and Hou [10], and also in the subgrid upscaling approach by Arbogast [7, 4].

**3.3. Properties of the MsMFEM approximation.** We now proceed to verify that the MsMFEM approximation $v_{\text{ms}}$ obtained from the local approach in Section 3.2.1 and from the basis functions for pressure given in (3.6), is conservative on the fine grid $\mathcal{K}$. By this, we mean that for any $K_m \in \mathcal{K}$, the total out-flux over the faces of $K_m$ should equal the source in $K_m$, or equivalently by the divergence theorem

$$\int_{\partial K_m} v_{\text{ms}} \cdot \nu \, ds = \int_{K_m} \nabla \cdot v_{\text{ms}}(x) \, dx = \int_{K_m} q(x) \, dx. \tag{3.7}$$

Let now $\{\psi_{ij}\}$ denote approximations to the basis functions (3.4) obtained from a conservative method, i.e., a finite-volume method or a mixed finite-element method. It follows that if $T_i$ is the unique coarse cell that contains $K_m$, then we have $\int_{K_m} \nabla\cdot\psi_{ij} = \int_{K_m} w_i$. For $x \in T_i$ we have $v_{\text{ms}}(x) = \sum_j v_j \psi_{ij}(x)$. Then by the definition of the pressure basis-functions (3.6) it follows from (3.2) that

$$\int_{T_i} q \, dx = \int_{T_i} \nabla \cdot v_{\text{ms}} \, dx = \sum_j v_j \int_{T_i} \nabla \cdot \psi_{ij} \, dx = \sum_j v_j \int_{T_i} w_i \, dx = \sum_j v_j.$$

By joining these fine-scale and coarse-scale conservation properties, we obtain

$$\begin{aligned} \int_{K_m} \nabla \cdot v_{\text{ms}}(x) \, dx &= \sum_j v_j \int_{K_m} \nabla \cdot \psi_{ij} \, dx \\ &= \int_{T_i} q(x) \, dx \; \cdot \; \int_{K_m} w_i \, dx = \int_{K_m} q(x) \, dx. \end{aligned} \tag{3.8}$$

Here the last equality follows from (3.5) if $T_i$ contains a source, and from the fact that $\int_{T_i} q = \int_{K_m} q = 0$ otherwise. Note that a prerequisite for this result to hold is that the source distribution $w_i$ is the same for all basis functions with support in $T_i$.

It has been argued (see [1, 2, 3]) that if one alters the velocity base functions to produce conservative velocity fields on a subgrid scale, it is also necessary to alter

the approximation space for pressure. However, one can justify the present choice of approximation space by arguing that the MsMFEM solution $v_{\text{ms}}$ for velocity remains the same for all approximation spaces $V \subset \mathcal{P}_0(\mathcal{K})$ that admit a unique solution such that the resulting $v_{\text{ms}}$ is conservative on the fine grid. Here $\mathcal{P}_0(\mathcal{K})$ denotes the space of piecewise constants on the fine grid.

To see this, suppose that $(v'_{\text{ms}}, p') \in U_{\text{ms}} \times V'$ solves (3.1)–(3.2) with $V$ replaced by another approximation space $V' \subset \mathcal{P}_0(\mathcal{K})$, and that $v'_{\text{ms}}$ is conservative on the fine grid, i.e., $\int l\nabla \cdot v'_{\text{ms}} = \int lq$ for all $l \in \mathcal{P}_0(\mathcal{K})$. Then, since $\lambda K$ is bounded and positive definite, there exists $\alpha > 0$ such that $\alpha|\xi|^2 \leq \xi \cdot (\lambda K)^{-1}\xi$ for all $\xi \in \mathbb{R}^d$. It follows from (3.1) that

$$\begin{aligned} \|v_{\text{ms}} - v'_{\text{ms}}\|^2 \alpha &\leq \int_\Omega (v_{\text{ms}} - v'_{\text{ms}}) \cdot (\lambda K)^{-1}(v_{\text{ms}} - v'_{\text{ms}})\, dx \\ &= \int_\Omega (p - p')\nabla \cdot v_{\text{ms}}\, dx - \int_\Omega (p - p')\nabla \cdot v'_{\text{ms}}\, dx = 0, \end{aligned} \tag{3.9}$$

and hence that $v'_{\text{ms}} = v_{\text{ms}}$. Note also that if the global velocity solution $v$ computed on the fine grid lies in $U_{\text{ms}}$, then $v_{\text{ms}} = v$. Thus, since we are only interested in an approximation for the velocity, and the MsMFEM solution $v_{\text{ms}}$ is independent of the choice of compatible approximation spaces for pressure, we choose for practical reasons a simple approximation space that allows an efficient implementation.

REMARK 1. *The pressure equation is coupled to time-dependent saturations through the mobility $\lambda(S(x,t))$. A crucial part of making the MsMFEM efficient is an adaptive updating procedure for the basis functions, in which we only update basis functions in regions where the saturation has changed substantially. This generally implies that only a small portion of the basis functions need to be recomputed at each time step. This adaptive updating process has been applied by Jenny et al. [20, 21] and by Aarnes [1]. We also remark that the method in general performs well even without updating, as long as the global boundary conditions do not change. This is discussed for the multiscale finite-volume method by Efendiev et al. [14].*

**4. Tuning the Local Basis Functions for Velocity.** In this section we discuss the choice of source distribution $w_i$ for the local basis functions introduced in Section 3.2.1. We also introduce a generalisation of the basis functions, which we will use when discussing the impact of nonconvex support domains.

**4.1. Source Distribution for the Local Velocity Basis Functions.** In [3] a uniform source term $w_i$ was used, except when $T_i$ contains a source or sink; that is:

$$w_i(x) = \begin{cases} q(x)/\int_{T_i} q(\xi)\, d\xi, & \text{if } \int_{T_i} q(x)dx \neq 0, \\ 1/|T_i|, & \text{otherwise.} \end{cases} \tag{4.1}$$

A problem with this choice of $w_i$ is that unnaturally high flow may be introduced in low-permeable regions. To illustrate, we consider a simple example (see Figure 4.1):

$$\begin{aligned} &\nabla \cdot k\nabla p = 0, \quad \text{in } \Omega_{ij} = (0,1)^2, \\ &p(0,y) = 1, \quad p(1,y) = 0, \quad \partial_y p(x,0) = \partial_y p(x,1) = 0, \end{aligned}$$

where $k(x,y) = k_l$ for $y < 1/2$ and $k(x,y) = k_h$ for $y \geq 1/2$. The unique velocity solution $v = -k\nabla p$ to this problem is given by

$$v(x,y) = \begin{cases} v_l = (k_l, 0)^T, & y < 1/2 \\ v_h = (k_h, 0)^T, & y \geq 1/2. \end{cases} \tag{4.2}$$

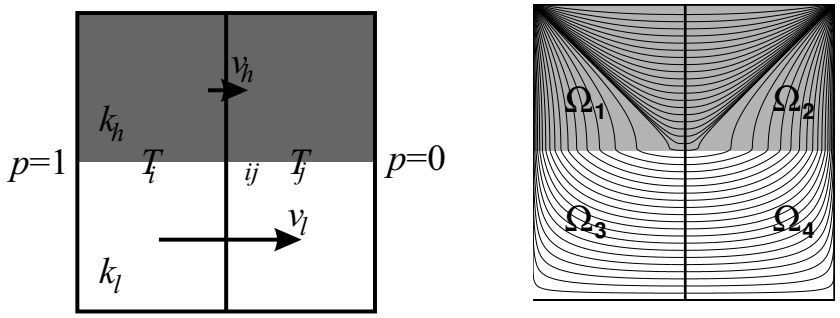


FIG. 4.1. *Schematic of a layered structure that traverses two neighbouring grid blocks. The left figure shows the type of flow that one would get if the two-block domain is subjected to a constant pressure drop in the horizontal direction. The right figure shows the corresponding streamlines induced by the MsMFEM basis function with constant source.*

We now compare this solution with the corresponding basis function $\psi_{ij}$ of (3.4) with uniform source $w_j = w_i = 1/|T_i| = 2$. For a given velocity $v$, let $f_h(v)$ and $f_l(v)$ be the corresponding fluxes across the top and bottom half of $\Gamma_{ij}$, respectively. For the true solution $v$ defined by (4.2) we see that the associated flux ratio is given by $f_h(v)/f_l(v) = k_h/k_l$. In contrast, $f_h(\psi_{ij})/f_h(\psi_{ij})$ is bounded above and below by 3 and 1/3, respectively (see Appendix A for an argument).

This example shows that the MsMFEM using uniform sources may produce significant local errors in the velocity field if large permeability contrasts penetrate the coarse-grid interfaces. Indeed, this follows by recalling that $v_{\text{ms}}$ is a superposition of the basis functions, and noting that $\psi_{ij}$ is the sole basis function that gives a flux contribution across $\Gamma_{ij}$.

To remedy this cause of error, we suggest to let the source distributions scale in accordance to the permeability. Thus, we let

$$w_i(x) = \begin{cases} q(x)/\int_{T_i} q(\xi)\, d\xi, & \text{if } \int_{T_i} q(x)dx \neq 0 \\ \sigma(x)/\int_{T_i} \sigma(\xi)\, d\xi, & \text{otherwise,} \end{cases} \tag{4.3}$$

where $\sigma(x)$ is some average of the permeability tensor $K(x)$. Through numerical testing we have settled on the arithmetic average:

$$\sigma(x) = \text{trace}(K(x))/d, \tag{4.4}$$

where $d$ is the number of space dimensions and trace$(A)$ denotes the sum of the diagonal entries of the matrix $A$ and equals the sum of the eigenvalues. Thus for an anisotropic tensor, high-permeable directions are weighted stronger than low-permeable directions. We also considered geometric and harmonic averages, but the best results were obtained from the selection (4.4). This indicates that the most important factor for the source distribution $w_i$ is capturing high-permeable directions. A numerical experiment comparing constant versus scaled source-terms is presented in Section 6.1.

**4.2. Support Domains for the Local Velocity Basis Functions.** In Section 3.2.1 we defined the support domain of a basis function $\psi_{ij}$ as $\Omega_{ij} = T_i \cup \Gamma_{ij} \cup T_j$. For general coarse grids, the domains $\Omega_{ij}$ may have arbitrary shapes, and singularities at reentrant corners of nonconvex domains may occur in the corresponding analytical solutions. Consider Figure 4.2. In the top-left plot we clearly see the artifact of

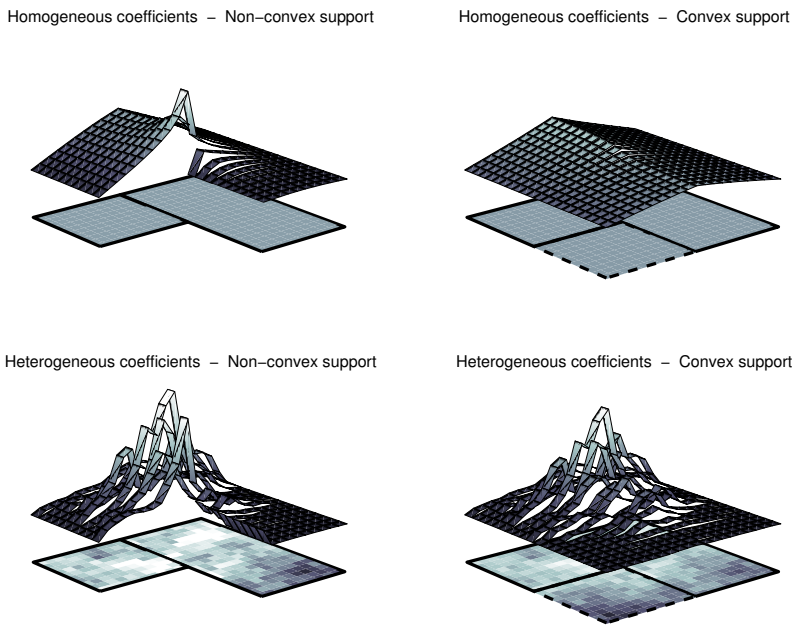


FIG. 4.2. *Velocity basis function associated with an edge between two cells of different size in 2D. The plots show the x-component for four different cases with homogeneous/heterogeneous coefficients and convex/nonconvex support.*

the reentrant corner as a peak in the velocity field, and this may induce an error if for example the true flow is uniform across the interface. In the top-right plot we have extended the support domain, and the peak vanishes. To be precise, we chose a convex $\Omega_{ij}$ that contained $T_i$ and $T_j$, and computed $\psi_{ij}$ from

$$\psi_{ij} = -\lambda K \nabla \phi_{ij}, \quad \nabla \cdot \psi_{ij} = \begin{cases} w_i(x), & \text{for } x \in T_i, \\ -w_j(x), & \text{for } x \in T_j, \\ 0, & \text{otherwise,} \end{cases} \tag{4.5}$$

with $\psi \cdot \nu_{ij} = 0$ on $\partial\Omega_{ij}$. (We note that also this definition of basis functions results in a conservative velocity field on the fine grid.) For special situations with uniform flow perpendicular to the coarse edges, we are able to reproduce the flow exactly on nonuniform grids through extending the support domains. For more complicated flow-scenarios, however, extensive numerical experiments have shown that the selection of convex versus nonconvex domains does not seem to be of great importance, even though the basis functions analytically have singularities. For heterogeneous non-continuous coefficients, which is the typical case in reservoir simulation, one can argue that the analytical solution will in any case have singularities due to jumps in the permeability field around corners of the fine-grid cells. We therefore believe that extending the support-domains of the basis functions is not worth the loss of flexibility and the extra work due to stronger coupling in the resulting coarse system. In Section 6.2 we present a numerical example that illustrates this claim. Thus,

for all the other experiments presented in Section 6, we use *tight* support; that is, $\Omega_{ij} = T_i \cup \Gamma_{ij} \cup T_j$.

REMARK 2. *Chen and Hou [10] employed an oversampling strategy to reduce resonance errors caused by improper boundary conditions; that is, by extending the support domain to include a border region around the coarse grid blocks, they were able to improve the convergence results. Unfortunately, the corresponding MsMFEM will no longer be conservative (at least not without modification) since the subgrid fluxes will not match across coarse-grid interfaces in general. In addition the use of enlarged support domains increases the computational effort. For these reasons, we here refrain from using an oversampling strategy.*

**5. High-Quality Grids.** The notion of high-quality grids is used in many applications, but often with different meanings. Roughly speaking, a high-quality grid for numerical modelling should resolve the main features of the physical phenomena of interest by introducing grid refinement only when it is required by nature, for instance to track the tip of a crack propagating through a solid. For porous media flows it is often acknowledged that it is important to have grids that properly account for anisotropy and dominating heterogeneity structures. For instance, in layered reservoir formations it is customary to use grids with coordinate directions along, and perpendicular to the layers. This convention allows one to model the interface between the layers accurately and express the permeability of the media using a diagonal tensor. If, on the other hand, the layers are tilted relative to the coordinate system for an orthogonal Cartesian grid, a full tensor will be needed to represent the permeability, and grid refinement would be needed to correctly model the interfaces between the layers.

Although a grid of high quality for the MsMFEM should obey the same physical principles, one should keep in mind that in our case we always have a fine sub-grid. Thus, local grid refinement on the coarse grid, for example, does not need to have the same effect for the MsMFEM as for standard FEMs. By construction, the MsMFEM is meant to capture small-scale heterogeneities through the use of multiscale basis functions. However, if these basis functions are to capture the fine-scale properties, their support domain cannot be too small (i.e., must contain sufficiently many fine-grid cells). Thus, excessive coarse-grid refinement may destroy the subscale resolution property. This observation has more theoretical foundations in the homogenisation results in [10], which show that the error estimates of the original method are weakened as the mesh size of the coarse grid approaches the scale of periodicity in the media. Thus, the coarse grid should not be refined due to small-scale features, but rather be refined or adapted to large-scale features of importance.

In the grid-generation procedures we propose here, it is implicitly assumed that the grid that models the porous medium at the subgrid scale is a suitable grid for accurate flow simulation. The aim is then to define a coarse grid for the MsMFEM, meaning that each grid block consists of a subfamily of the fine-grid cells, such that one strikes a balance in capturing features at all scales that effect the important characteristics of the flow scenario. Thus, we need to define what we consider as important characteristics. For the nonuniform coarsening approach, Durlofsky et al. [13] required agreement in

- the global flow-rate behaviour of the reservoir,
- the breakthrough characteristics of the displacing fluid,
- the post-breakthrough fractional flows of the reservoir fluids.

The authors demonstrated that if these requirements were satisfied for one-phase

flow (or for two-phase flows with unit mobility ratio), the model usually performed well, also for simulation of two phases with a low or moderate mobility ratio. As we shall see in the numerical experiments in Section 6, this also translates to our case. One big difference in our setting, though, is that the MsMFEM produces a detailed velocity field on the fine grid, and thus a direct comparison with a fine-scale solution is possible. However, requiring that the MsMFEM should match the reference solution at a detailed level is rather strict, and in any case not necessary to satisfy the above requirements.

Thus ideally, a high-quality coarse grid for the MsMFEM should adapt to the large-scale features of importance for the flow scenario, while small-scale heterogeneities should be resolved in the basis functions. In addition, we restrain the bandwidth of the discretisation matrix $\mathbf{B}$ in (3.3) by requiring that the number of neighbours for any coarse block is bounded and preferably small. The next subsection describes a block-splitting strategy to make the coarse grid adapt to barriers and cross-flow. A more direct approach for the case of barriers, is described in the numerical examples of Sections 6.3 and 6.5.

**5.1. A Coarse-Grid Refinement Procedure.** To generate a (nonuniform) coarse grid for the MsMFEM we start with an arbitrarily given coarse grid and perform some sort of refinement until the grid satisfies the selected criteria for a high-quality grid. As for the basis functions, we distinguish between a local and a global approach, where the global approach uses an initial fine-grid velocity field. Below we outline two alternative refinement strategies. The first approach is independent of the flow process and does not require computing $v$. The second approach, which is case-oriented, exploits information about fine-scale flow patterns to avoid unnecessary refinement. Hence, we consider two different approaches:

- *Static grid refinement:* In this approach the coarse grid is held constant, also if boundary values and and/or well configurations change.
- *Dynamic grid refinement:* In this approach the coarse grid is regenerated when boundary values or well configurations change.

Both procedures employ two different refinement criteria.

The first and most important criterion, which attempts to ensure that the MsMFEM does not force too much flow through low-permeable flow barriers, is the same for both methods. This criterion is described and motivated in Section 5.2.

In the second criterion it is recognised that difficulties occur if we have large flow velocities in opposite directions across $\Gamma_{ij}$. This situation can occur in e.g., fluvial porous formations, where the predominant flow tends to follow narrow high-permeable flow channels. A criterion that attempts to detect cross-flow across interfaces is discussed in Section 5.3. Here an initial fine-scale velocity field is assumed in the dynamic approach, while the static approach uses local flow computations.

**5.2. Flow Across Low-Permeable Barriers.** If a low-permeable wall, e.g., a shale barrier, traverses a coarse grid block $T_i$, the local version of the MsMFEM may produce an unnatural amount of flow through the barrier, even with the alternative definition of the source distribution terms from Section 4.1. This is an artifact caused since we impose no-flow boundary conditions on the boundary of the support domains. To illustrate how flow barriers of this type may affect the MsMFEM solution, consider the two examples shown in Figure 5.1. In the first example a low-permeable barrier with permeability $10^{-10}$ mD traverses a block $T_i$ with a homogeneous background permeability of 1 mD. In the second example the low-permeable region traverses the block only partially. The corresponding basis functions are illustrated with vector

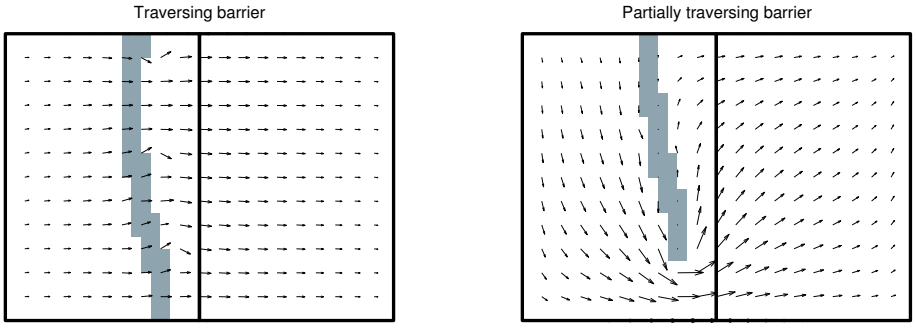


FIG. 5.1. *Vector plots of 2D basis functions. Flow being forced through a barrier (left), and going around a barrier (right).*

plots. We see that high flow is forced through the barrier only in the first example. Indeed, in this case the flow on the left side of the barrier has no other escape route than to pass through the barrier. For the second case we see that the base function neatly allows the flow to go around the barrier. To define a criterion that detects flow barriers, while at the same time is able to distinguish between the two cases considered in the previous examples, consider the quantity

$$\upsilon_{ij} = \psi_{ij} \cdot (\lambda K)^{-1} \psi_{ij}. \tag{5.1}$$

For the above example, the basis function with the traversing barrier attains a maximum of size $\mathcal{O}(10^{10})$ for $\upsilon_{ij}|\Gamma_{ij}|$ , while in the case of the partially traversing barrier, the corresponding value is of size $\mathcal{O}(1)$. Recall that the diagonal entry associated with $\psi_{ij}$ in the matrix-block $\mathbf{B}$ in (3.3) is given by $b_{ij,ij} = \int_\Omega \upsilon_{ij}\, dx$. The examples considered above suggest that extremes in the indicator function $\upsilon_{ij}$ signifies that a flow barrier is present, and that the MsMFEM fails to model the local displacement across the edge $\Gamma_{ij}$ properly. This situation leads to extreme diagonal entries in $\mathbf{B}$, which in turn will cause the MsMFEM to underpredict the flow across $\Gamma_{ij}$. Thus, to get a more correct velocity field we perform a grid refinement in $T_i$. That is, if for some prescribed constant $C$, we have

$$\max_{x \in T_i} [\upsilon_{ij}(x)]\, |\Gamma_{ij}| > C, \tag{5.2}$$

then $T_i$ is split into two new blocks $T_k$ and $T_l$, such that the new interface $\Gamma_{kl}$ is approximately parallel to the "old" interface $\Gamma_{ij}$. We note that by applying this splitting iteratively, we will not necessarily get rid of the extremes (5.1), but they will only appear for basis functions with small support.

**5.3. Detecting Alternate Directions of Flow Across Coarse Edges.** The local MsMFEM basis functions are characterised by a unit total flux across the respective coarse-grid interfaces. Thus, if the true positive and negative fluxes across $\Gamma_{ij}$ are of the same magnitude, i.e., if

$$\int_{\Gamma_{ij}} \max(v \cdot \nu, 0)\, ds \approx -\int_{\Gamma_{ij}} \min(v \cdot \nu, 0)\, ds,$$

then it becomes particularly difficult to obtain a good match between $v_{\text{ms}}$ and $v$ on $\Gamma_{ij}$. This situation can occur if e.g., a high-permeable channel enters and exits

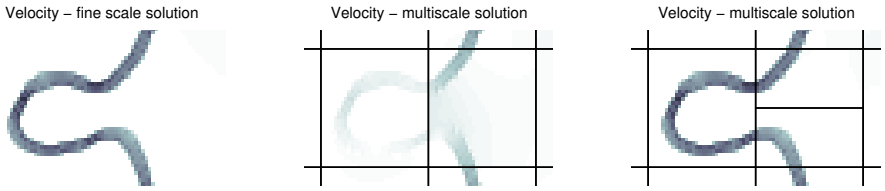


FIG. 5.2. *Part of a velocity field computed on the fine grid (dark regions indicate high absolute velocity). The coarse-grid solution (middle), can only reproduce this flow scenario after a refinement (right).*

$T_i$ through $\Gamma_{ij}$ as depicted in Figure 5.2. We will refer to situations with flow in opposite directions as cross-flow. The use of global basis functions (Section 3.2.2) will, in principle, resolve cross-flow across interfaces, but can be sensitive to small perturbations in the flow conditions on faces with large cross-flow and total flux close to zero.

The problem with cross-flow for the local basis functions is demonstrated in Figure 5.2. The figure also demonstrates that we are able to produce an accurate flow scenario by inserting an extra edge in $T_j$ and using the MsMFEM with local basis functions defined by (3.4). Indeed, neither of the two new interfaces on the 'old' interface are now subjected to cross-flow. If cross-flow occurs on a coarse-grid interface $\Gamma_{ij}$, the total flux across $\Gamma_{ij}$ may be small even though the magnitudes of the corresponding fine-scale fluxes are not. Thus, to detect cross-flow over coarse-grid interfaces we will use the following criterion:

$$\left| \int_{\Gamma_{ij}} v \cdot \nu \, ds \right| \ll \int_{\Gamma_{ij}} |v \cdot \nu| \, ds \quad \text{and} \quad C < \int_{\Gamma_{ij}} |v \cdot \nu| \, ds. \tag{5.3}$$

The second inequality is introduced to avoid refinement where cross-flow is apparent, but where the absolute total flux is too small to have a global impact. We now discuss what type of refinement procedure is most appropriate for making the MsMFEM resolve flow scenarios with cross-flow over interfaces.

To simplify the discussion of the splitting strategy, let $\mathcal{T}$ be a regular partitioning of $\Omega \subset \mathbb{R}^3$ into hexahedrons, and consider a face $\Gamma_{ij} = \partial T_i \cap \partial T_j$ with normal vector parallel to the $x$-axis, i.e.,

$$\Gamma_{ij} = \{(x, y, z) \in \Omega \, : \, x = x_0, \; y_0 < y < y_1, \; z_0 < z < z_1\}.$$

If the inequality (5.3) is satisfied for $\Gamma_{ij}$ for some given threshold, we consider either splitting $\Gamma_{ij}$ vertically or horizontally by splitting either $T_i$ or $T_j$ into two blocks. For example we perform a horizontal splitting if the inequality

$$\left| \int_{y_0}^{y_1} \int_{z_0}^{z_1} (v(x_0, y, z) \cdot n) dz dy \right| < C_1 \int_{z_0}^{z_1} \left| \int_{y_0}^{y_1} (v(x_0, y, z) \cdot n) dy \right| dz \tag{5.4}$$

holds for some given threshold $C_1$. From this formulation it is not given which of the two blocks, $T_i$ or $T_j$, should be split, and in the numerical experiments we performed, the splitting was chosen randomly. A more sophisticated approach to minimise the amount of refinement could be applied, but for the purposes of this paper we settled on the above. One such splitting is illustrated in Figure 5.3. If a global fine-scale

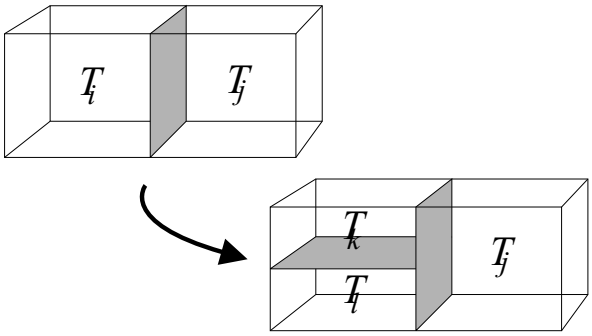


FIG. 5.3. *Horizontal splitting of the block $T_i$.*

velocity field is not attainable, one can consider a localised version of the above: Consider again the face $\Gamma_{ij}$ from above, and let $v^y = -K\nabla p^y$ be the velocity field obtained from the local flow problem

$$\nabla \cdot v^y = 0, \text{ in } \Omega_{ij}, \tag{5.5}$$

subject to

$$\begin{aligned} p^y &= 1, \text{ on } \Gamma_{y_0}, \\ p^y &= 0, \text{ on } \Gamma_{y_1}, \\ v^y \cdot \nu &= 0, \text{ on } \partial\Omega_{ij} \setminus (\Gamma_{y_0} \cup \Gamma_{y_1}). \end{aligned} \tag{5.6}$$

Here $\Gamma_{y_0}$ and $\Gamma_{y_1}$ denote the two faces of $\partial\Omega_{ij}$ parallel to the $xz$-plane. If the inequality (5.4) is satisfied for the velocity field $v^y$, and the total absolute flow across the edge is larger than some fraction of the total flow through the localised model, it is likely that cross-flow can also appear for the global solution, and thus a splitting is performed. Through this procedure we are able to identify edges with potential cross-flow, although the local approach above is not quite as reliable as using an initially computed fine grid velocity field. Both the global and the local approaches are illustrated in the numerical examples in Section 6.4.

**6. Numerical Experiments.** In the following numerical experiments, our main objectives are to test the proposed scaling of source terms in the MsMFEM basis functions (from Section 4.1) and to illustrate our proposed refinement strategies. Thus, in an attempt to eliminate causes of error not directly relevant for these issues, we do not use adaptive updating of basis functions (Remark 1), but rather update all basis functions every time step. We also assume for simplicity that porosity is equal unity everywhere in $\Omega$. All time units are in PVI (pore volumes injected), which in the unit porosity case is equal to the total amount of injected water divided by the total volume of the model.

In the experiments we use both linear and nonlinear relative permeability curves. In the linear case we use

$$k_{rw} = S, \qquad k_{ro} = 1 - S, \tag{6.1}$$

with initial saturation $S_0 = 0$ and viscosities $\mu_w = \mu_o = 1\,cP$. In the nonlinear case we use

$$k_{rw} = (S^*)^2, \qquad k_{ro} = (1 - S^*)^2, \qquad S^* = \frac{S - S_{wc}}{1 - S_{wc} - S_{or}}, \tag{6.2}$$

with $S_{wc} = S_{or} = 0.2$, viscosities $\mu_o = 3.0\,cP$ and $\mu_w = 0.3\,cP$, and initial saturation $S_0 = S_{wc}$. Note that in the linear case, the total mobility does not change over time, and thus the velocity needs to be computed only once. In this case, the use of global basis functions (Section 3.2.2) makes no sense, since it will only reproduce the reference solution. In all examples, the reference solution is computed directly on the fine grid by a mixed finite-element method using the lowest-order Raviart–Thomas elements.

For the saturation equation (2.4), we use a conservative scheme on the following form:

$$S_i^{k+1} = S_i^k + \frac{\triangle t}{|K_i|}\left(Q_i(S^m) - \sum_{j\neq i} F_{ij}(S^m)v_{ij}\right), \qquad m = k, k+1. \tag{6.3}$$

Here $\triangle t$ denotes the time step and $|K_i|$ is the measure of grid cell $K_i$ (in the fine grid $\mathcal{K}$). Furthermore, $Q_i(S) = \int_{V_i} q_w(S)$ is the source contribution in $K_i$, and

$$F_{ij}(S) = \max\{\operatorname{sign}(v_{ij})f_w(S_i), -\operatorname{sign}(v_{ij})f_w(S_j)\}$$

is the upstream-weighted fractional flow function for $\gamma_{ij} = \partial K_i \cap \partial K_j$. Finally, $v_{ij} = \int_{\gamma_{ij}} v \cdot n_{ij}\,ds$, where $n_{ij}$ is the unit normal to $\gamma_{ij}$ pointing from $K_i$ to $K_j$. In the explicit case ($m = k$) this type of scheme requires a CFL condition, which may put severe restrictions on the time steps. For large problems arising in, for instance, oil reservoir simulation, it is therefore customary to use an implicit scheme ($m = k + 1$) with a Newton–Raphson solver. In this paper, however, our primary focus is on the pressure equation, and the assumption of unit porosity allows us to use the more accurate explicit scheme.

**6.1. Source Terms for the Basis Functions.** In Section 4.1, we argued that scaling the source terms in the basis functions would give more correct flow over coarse edges. In this experiment we consider a 3D subsample of Model 2 from the 10th SPE Comparative Solution Project [11]. The model consists of $40 \times 40 \times 12$ fine-grid blocks from the top corner of the full model, and we introduce a source in cell $(1, 1, 1)$ and a corresponding sink in cell $(40, 40, 12)$. The initial saturation is $S_0 = 0$, and we use linear relative permeability curves (6.1). We note that this is a difficult test case as the flow is being forced vertically through several horizontal layers.

Let $v_{\text{ref}}(t)$ be the reference velocity computed on the fine grid, and let $v_{\text{ms}}(t)$ denote the velocity field computed by the MsMFEM. There are a number of ways to compare the two velocity fields, but for reservoir simulation the most crucial factor is the transport properties of a velocity field. That is, a large local error in the velocity field may not be crucial as long as the overall transport properties are correct. Figure 6.1 shows four different error measures for the multiscale velocity field $v_{\text{ms}}$ computed on ten different coarse grids (given on the $x$-axes).

As a direct measure of the error in the computed velocity field, we consider the $L^2$-norm and the *energy*-norm:

$$\|v\|_2 = \left(\int_\Omega v \cdot v\; dx\right)^{\frac{1}{2}}, \qquad \|v\|_E = \left(\int_\Omega v \cdot (\lambda K)^{-1} v\; dx\right)^{\frac{1}{2}}, \tag{6.4}$$

where the corresponding relative errors are given as $\|v_{\text{ref}} - v_{\text{ms}}\|/\|v_{\text{ref}}\|$. The energy norm is perhaps the most natural choice, since the original problem (2.3) is equivalent

to the minimisation problem

$$\min_{v \in H_0^{\mathrm{div}}} \|v\|_E, \qquad \text{for } \nabla \cdot v = q$$

To assess the transport properties of the computed velocity field, we compare the induced saturation profiles. Let $S_{\mathrm{ref}}(x,t)$ and $S_{\mathrm{ms}}(x,t)$ be the saturations obtained from the reference and from the multiscale velocity fields, respectively. We then measure the relative difference in these saturation profiles at a given time $t$:

$$\frac{\int_\Omega |S_{\mathrm{ref}}(x,t) - S_{\mathrm{ms}}(x,t)| \; dx}{\int_\Omega |S_{\mathrm{ref}}(x,t) - S_{\mathrm{ref}}(x,0)| \; dx}. \tag{6.5}$$

Finally, we consider the watercut, i.e., the fraction of water in the produced fluid. Here we measure the maximal error, that is

$$\max_{0 \le t} |f(S_{\mathrm{ref}}(x_{pw},t)) - f(S_{\mathrm{ms}}(x_{pw},t))|, \tag{6.6}$$

where the saturations are evaluated at the midpoint $x_{pw}$ of the producing well in grid cell $(40, 40, 12)$. Note that this is a quite strict measure, since the watercut curves tend to be steep right after breakthrough, and thus a small deviation in breakthrough time may give a large value in the error measure (6.6).

The plots in Figure 6.1 show that computations with scaled source terms are more accurate in all four error measures, and in particular for the saturation error at time $t = 0.5$ PVI (saturation errors measured at other times $t$ gave similar plots). For this particular example, it appears as if the errors in energy norm and in saturation are correlated. However, in our experience the error in energy norm depends strongly on the given flow process and a prediction based on this error is only reliable if the error is small. In other words, a large error in energy norm does not necessarily mean a large error in the saturation profile.

Through this, and also several other test cases, we have seen that scaling the source terms improves the accuracy of the MsMFEM solution, even for high anisotropy ratios (the current case has anisotropy ratios up to $\mathcal{O}(10^4)$). The scaling strategy is applied in the remaining numerical examples of this paper. Note, however, that scaling the source terms has no effect for the global basis functions discussed in Section 3.2.2 since the MsMFEM solution is completely determined by the boundary conditions of the basis functions.

It is also worth noting that the MsMFEM using scaled source terms in this example performs well for all grids, and thus one would not gain much through local grid refinement. It also illustrates the fact discussed earlier: that the accuracy of the MsMFEM does not necessarily increase with decreasing coarse mesh size.

**6.2. A Comparison of Support Domains.** We now compare the use of convex versus nonconvex support domains for the MsMFEM base functions, as discussed in Section 4.2. Also in this example we use linear relative permeability (6.1), and thus the velocity field is computed only once.

First, we consider a homogeneous 2D model consisting of $60 \times 220$ fine-grid blocks, where a source and a sink are introduced in cells $(1,1)$ and $(60, 220)$, respectively. The MsMFEM is now applied to three different coarse grids (see Figure 6.2), where both convex and nonconvex support for the velocity basis functions are applied. In the convex case, we use the smallest bounding box with sides parallel to the $x$- and $y$-axes, and in the nonconvex case we use the union of the two neighbouring cells. The

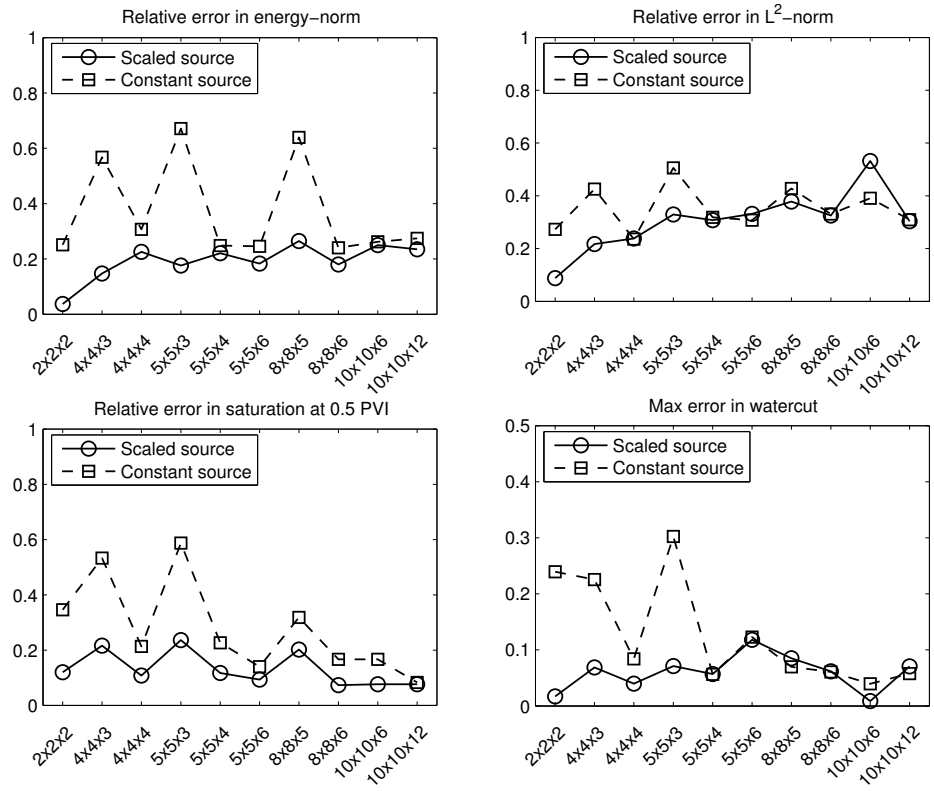


FIG. 6.1. *Four different measures of error for the MsMFEM computed with scaled and constant source terms.*

saturation profiles at 0.6 PVI for the two approaches are plotted in Figure 6.2. We see that the choice of grid clearly has an impact on the MsMFEM solution, but it is not evident that using convex support for the basis functions is superior to using nonconvex support.

We now repeat the above experiment, but replace the homogeneous permeability with a heterogeneous field taken from the top layer in the SPE10 test case [11]. Again we see that the choice of support domain is not important for the MsMFEM approximation, as the method captures the main features of the reference solution for all three grids regardless of the choice of support. Although reentrant corners in support domains can induce unwanted numerical artifacts (as seen in Figure 4.2), we have not seen that these effects play a crucial role for the overall MsMFEM solution, neither in this example nor in several others we have investigated. Defining convex support domains for general grids (especially in 3D) can be difficult, and in addition it induces a stronger coupling in the stiffness matrix of the coarse grid. Therefore, enforcing convex support does not seem to be worth the extra effort, especially for strongly heterogeneous coefficients, which are our primary application.

**6.3. A 2D Example with Barriers.** In this numerical experiment we consider a synthetic $128 \times 128$ fine-grid permeability field with several barriers of permeability $10^{-8}$ relative to the homogeneous background permeability (see Figure 6.4). Water is injected in cell $(1, 1)$ at a constant rate and oil (and water) is produced in the

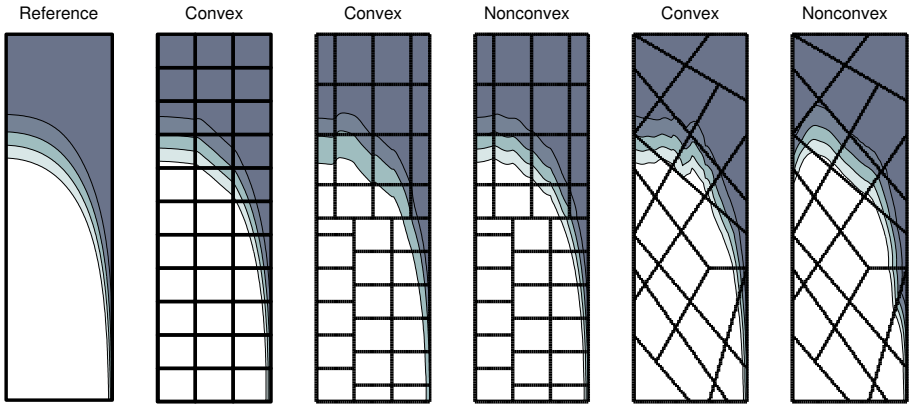


FIG. 6.2. *Saturation profiles at* 0.6 *PVI for the reference solution and several MsMFEM solutions for homogeneous coefficients.*

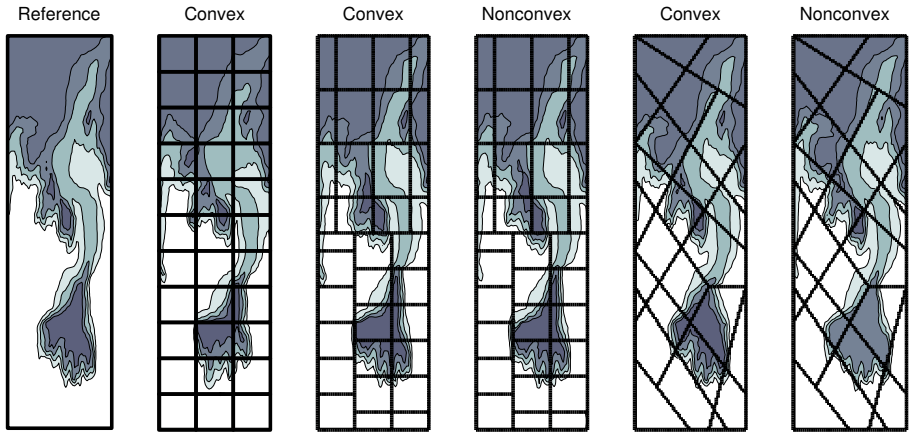


FIG. 6.3. *Saturation profiles at* 0.6 *PVI for the reference solution and several MsMFEM solutions for heterogeneous coefficients.*

opposite corner. In this experiment we use nonlinear relative-permeability functions (6.2) (the corresponding linear case (6.1) gave similar results and is not reported). We perform several MsMFEM computations, and compare with the reference solution obtained from the fine $128 \times 128$ grid. We apply the MsMFEM with (local) basis functions (3.4) on a $6 \times 6$ and on a $48 \times 48$ uniform grid, and then on the two nonuniform grids shown in Figure 6.5. The first grid consists of rectangular cells and is obtained automatically from applying condition (5.2) for detecting barriers iteratively and stopping the refinement when a coarse-grid cell reaches a size of three fine cells in each direction. This means that the smallest cells of the nonuniform grid are of about the same size as the cells in the uniform $48 \times 48$-grid. In addition the grid is regularised such that no cell has more than six active edges. We note that this is an illustrative example, and thus the amount of refinement is probably higher than what one would require in practise. The second nonuniform grid has grid-cells of more general shapes and is obtained from intersecting the uniform $6 \times 6$ grid with

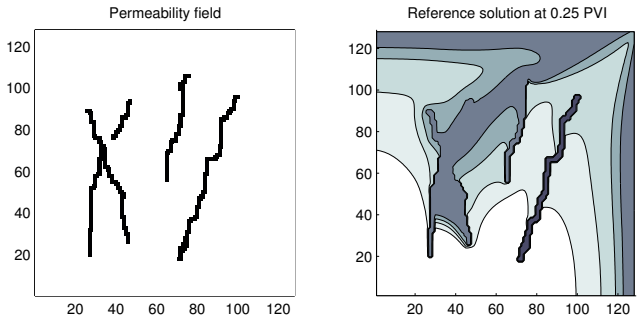


FIG. 6.4. *Permeability field, and saturation profile for the reference solution.*

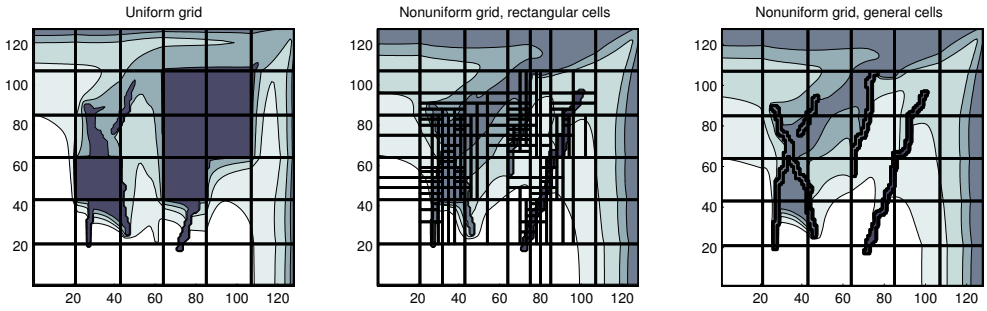


FIG. 6.5. *Saturation profiles obtained from the MsMFEM on different coarse grids.*

the exterior edges of the barriers.

The saturation profile for the reference solution is plotted in Figure 6.4. The corresponding profiles from the MsMFEM solution obtained on the coarse $6 \times 6$ grid and on the two nonuniform grids are depicted in Figure 6.5. On the uniform grid, several cells stay unsaturated due to the traversing barriers, as discussed in Section 5.2, and the multiscale method fails to produce the correct solution. The two nonuniform grids, on the other hand, capture the flow around the barriers correctly.

Watercut curves and saturation errors over time are shown in Figure 6.6. Although the watercut curve for MsMFEM on the uniform $6 \times 6$ grid is not far from the reference solution, the method clearly overpredicts the production of water, as one would expect from the unsaturated coarse cells in Figure 6.5. The plot of saturation errors clearly demonstrates the improvement obtained from using nonuniform grids. For comparison, we have also plotted the results from the global approach (Section 3.2.2) on a uniform $6 \times 6$ grid, for which the initial fine-scale solution is used to determine boundary conditions on the velocity basis functions. The global method performs excellent without any refinement. We have also plotted the saturation error on the coarse grid, which is the analogue when saturation is averaged back onto a uniform $6 \times 6$ grid.

Overall the uniform $48 \times 48$ grid gives the least error, which is to be expected since this particular problem only contains large-scale heterogeneities in the form of low-permeable barriers that are best resolved using a coarse grid that is as small as possible. Still, it is clear that both nonuniform grids are able to capture the reference flow in this example. It is worth noting that the nonuniform grid with grid cells obtained directly from the barriers performs slightly better than the automatically

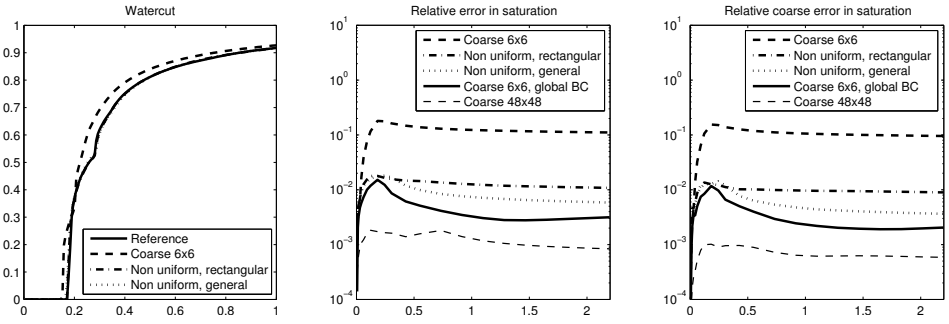


FIG. 6.6. *Watercut curves, fine- and coarse saturation errors for MSMFEM on various grids in the 2D barrier example.*

generated grid, even though it has a substantially smaller number of coarse-grid cells.

**6.4. A 2D Example With Cross-Flow.** We now consider a horizontal section of the SPE test case [11] (the top layer of the Upper Ness formation), see Figure 6.7. The section is characterised by a high permeability channel with sharp turns resembling the example in Figure 5.2. The initial $5 \times 11$ coarse grid is chosen deliberately so that the MsMFEM runs into trouble: if the coarse grid is placed on top of the reference solution, a large amount of cross flow will appear over a few coarse edges. An injector is placed in the centre of the model, and four equal producers are situated in the corners. We use nonlinear relative-permeability functions given by (6.2).

The MsMFEM is applied in four different ways:

- A $5 \times 11$ uniform grid, and local basis functions (Section 3.2.1).
- A nonuniform grid with local basis functions, where the refinement is performed in the local way described in Section 5.3.
- A $5 \times 11$ uniform grid with global basis functions computed with boundary conditions obtained from an initial fine-scale velocity field (Section 3.2.2).
- A nonuniform grid, where both the refinement (see Section 5.3) and the computation of the basis functions are performed based on the initial fine-scale solution.

Thus, the first two approaches are completely local in the sense that no knowledge of a fine-scale velocity field is utilised. The nonuniform grids are shown in Figure 6.7. The refinement is performed only for extreme values, and thus only four cells are split in the local approach. Two of the cell splittings occur where the high-permeable channel produces cross-flow over coarse edges, and thus the procedure is able to detect edges of potential cross-flow correctly. The other two splittings are performed in low-permeable regions where there is not much flow at all for the current flow pattern. Such splittings can hardly be avoided in a *local* approach, since no apriori information about flow patterns is available during the refinement procedure. In fact, being able to identify problem regions apriori makes the method more robust with respect to changes in the flow pattern as a result of e.g., changes in the well configuration due to infill drilling, etc.

Although the errors produced by the local version of the MsMFEM on the uniform grid are not too large, the improvement due to the four local splittings is evident. Figure 6.8 shows that refinement also improves the solutions obtained by the global version of the MsMFEM, even though these improvements are harder to spot by just looking at saturation profiles in Figure 6.7.

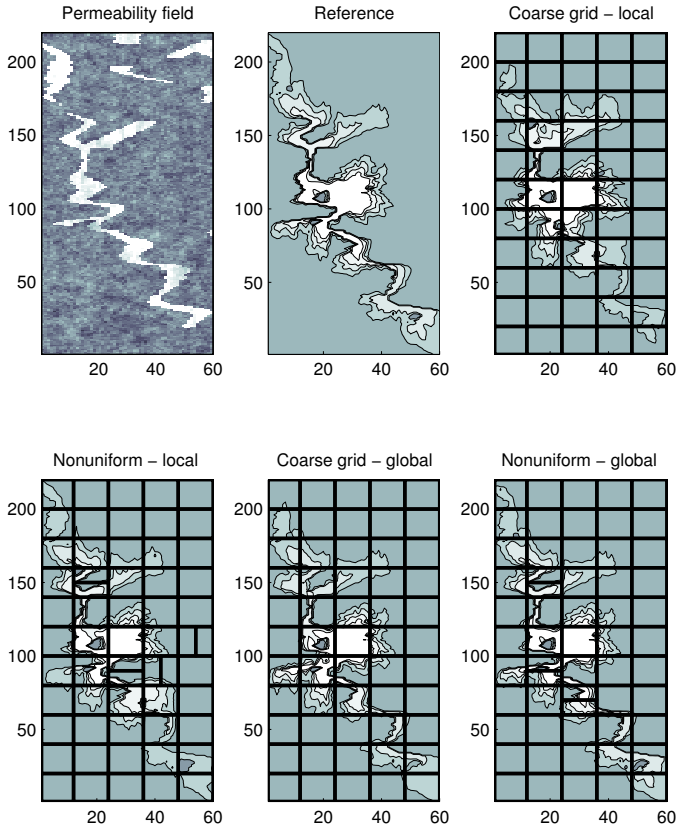


FIG. 6.7. *Permeability field and saturation profiles at* 0.12 *PVI.*

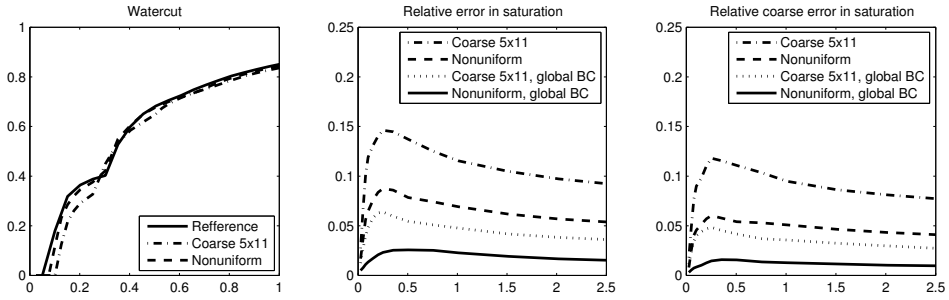


FIG. 6.8. *Watercut curves and saturation errors for various simulations in the cross-flow experiment.*

Through this experiment we see that cross-flow can have an impact on the MsMFEM solution and that we are able to correctly detect edges with potential problems. We note, however, that the impact of cross-flow on the MsMFEM seems to be less substantial than the impact of barriers. Especially in 3D, the flow-scenarios become so complex that it is difficult to find a case where cross-flow has a substantial impact on the MsMFEM solution. We return to this discussion in the concluding remarks of Section 7.

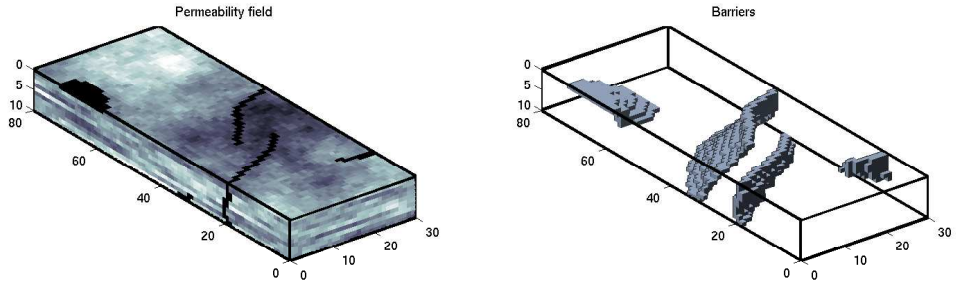


FIG. 6.9. *Permeability field (right), and the interior barriers (left).*

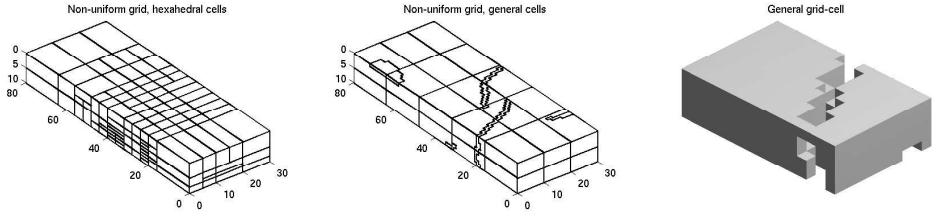


FIG. 6.10. *The two nonuniform grids used in the 3D experiment. To the right: one of the grid-cells in the second grid.*

**6.5. A 3D Example with Barriers.** In this experiment we once again consider a subsample of the SPE test case [11] consisting of $30 \times 80 \times 10$ fine-grid cells from the smoothly varying Tarbert formation, where we have introduced a few low-permeable walls ($10^{-8}$ mD). The permeability field and the barriers are plotted in Figure 6.9. A source is introduced along the vertical line at $(x, y) = (1, 1)$, and a corresponding sink at $(x, y) = (30, 80)$. The simulation is run with linear relative permeabilities (6.1).

As in the 2D experiment with barriers (Section 6.3), the low-permeable barriers can be detected automatically through the criterion (5.2). The resulting nonuniform grid with local refinement around the barriers is depicted in Figure 6.10. In the refinement procedure, we prescribed a minimum size for the coarse grid such that each coarse-grid cell should contain at least $4 \times 4 \times 1$ fine-grid cells, and a regularisation was performed to ensure that each cell has at most nine active faces. We also constructed a coarse grid by intersecting the faces of the barriers with a uniform $3 \times 5 \times 2$ grid as shown in Figure 6.10. On this grid no regularisation was performed, and one of the resulting grid-cells is also shown in Figure 6.10; the original $10 \times 16 \times 5$ hexahedral grid-cell is almost split in two by the barrier, and the resulting cell is only connected through a single fine-grid cell. One would perhaps expect that this situation would effect the resulting MsMFEM solution, but this is not the case.

As in Section 6.3, the MsMFEM solution obtained on the uniform coarse grid experiences problems around the barriers. This is illustrated in Figure 6.11, where we have plotted an isosurface of the saturation for the reference solution and for the uniform grid MsMFEM solution. Again we see that a few coarse grid-cells stay unsaturated, and thus the watercut is overpredicted, see Figure 6.12. Both the nonuniform grids produce watercut-curves in close agreement with the reference solution. The improvements over the uniform coarse solution are even more evident in the error-plots for fine-scale and coarse-scale saturations. We see that the nonuniform grid with hexahedral grid cells gives a bit better resolution than the general nonuniform grid,

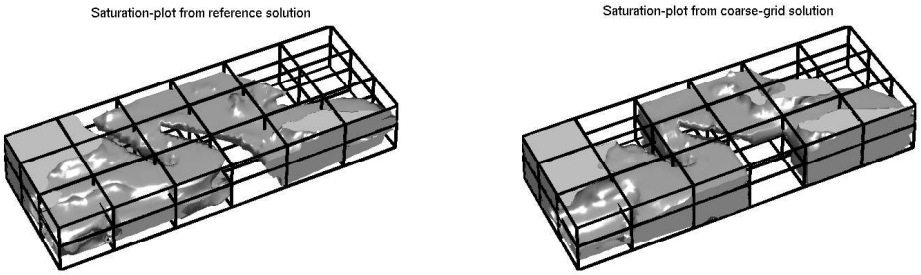


FIG. 6.11. *Waterflow through the model.*

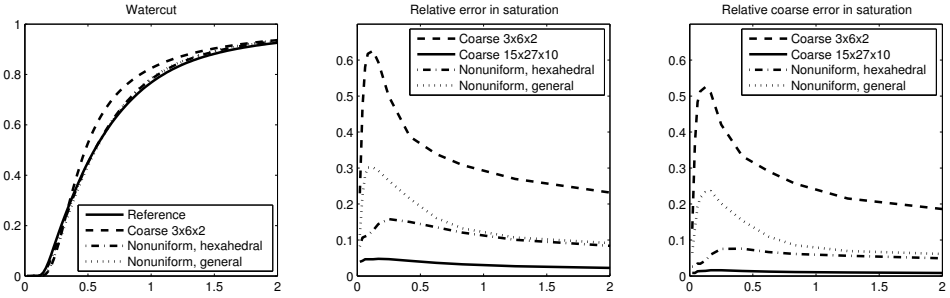


FIG. 6.12. *Watercut curves and saturation errors for various simulations.*

but then it also has almost five times as many grid cells (317 compared to 66).

**7. Concluding remarks.** The main focus of this paper has been to analyse and test the performance and capabilities of the MsMFEM on nonuniform and unstructured coarse grids. We have also improved the accuracy of the method by introducing a scaling of the source terms used to determine the multiscale basis functions for the velocity. We have pointed out two potential problem scenarios for the MsMFEM and suggested both a detection procedure and an amelioration strategy through splitting of coarse cells:

- **Traversing barriers.** We have seen that barriers traversing a coarse-grid cell may have the effect of zeroing the velocity in the entire cell. An automatic approach for detecting this situation based on extremes in the energy-norm of the corresponding basis functions is described. By iteratively splitting cells around barriers, we obtain improved solutions by ensuring that the flow barriers only traverse cells of small support in the coarse grid. An alternative approach, where coarse-grid cells constitute the actual barriers, is also presented, and improved results are obtained with only a moderate increase in the number of coarse cells. These strategies are illustrated for numerical experiments in both two and three spatial dimensions.
- **Cross-flow.** The way the current MsMFEM using local basis functions is defined, the relative distribution of fine-scale fluxes across a coarse edge is completely determined by the corresponding basis function. As a result, alternate directions of flux are hard to reproduce. Also in this situation one can split coarse cells to introduce an extra degree of freedom over the original coarse edge. Both a local and a global detection strategy for cross-flow is described.

We believe that the described strategies for improving the MsMFEM around barriers can be applied successfully to model fractures and faults also, for instance by including these irregular structures directly in a more regular coarse grid, but this is a topic for further study. Secondly, although we have addressed a problem with cross-flow for the MsMFEM, we do not believe that this situation is of great importance for real-life flow-scenarios. This conclusion is based on the fact that we have not been able to find a single non-synthetic 3D-case where cross-flow substantially effects the MsMFEM solution. Nevertheless, if the problem should occur, we have devised a procedure for detecting and fixing it.

Altogether we believe that the current multiscale method has a great potential for being applied to real-life flow simulations, in particular due to the great flexibility in choosing the coarse grid. The ability to include actual flow barriers directly in the coarse grid illustrates the great flexibility of the method in this respect. Being able to use coarse grids of an almost arbitrary shape immediately simplifies the usually complex process of choosing an appropriate coarse grid and upscaling and resampling petrophysical parameters like permeability and porosity.

**Appendix A.** In this appendix we prove the claim of the example in Section 4.1. We want to show that the flux ratio $f_l^h(\psi_{ij}) = f_h(\psi_{ij})/f_l(\psi_{ij})$ for the basis function $\psi_{ij}$ computed with constant source satisfies

$$\frac{1}{3} \leq f_l^h(\psi_{ij}) \leq 3, \tag{A.1}$$

independently of the ratio $k_h/k_l$ (see Figure 4.1), where the support-domain $\Omega_{ij}$ is the unit square, and $\Gamma_{ij}$ is at $x = \frac{1}{2}$. Let $\phi_{ij}$ be the pressure function of zero average such that $\psi_{ij} = -k\nabla\phi_{ij}$. By a change of variable $\tilde{x} = 1 - x$, one sees that $-\phi_{ij}(\tilde{x}, y)$ also solves (3.4), and thus $\phi_{ij}(x, y) = -\phi_{ij}(1-x, y)$. It follows that $\phi_{ij}$ is zero on $\Gamma_{ij}$, (and by the maximum principle) non-negative in $T_i$, and non-positive in $T_j$. Consider the upper left square $\Omega_1$. It has two edges with no flow, one edge (say $e_1$) with constant pressure equal zero, and one edge (say $e_2$) with pressure greater than or equal zero everywhere. Thus in $\Omega_1$, we can make the splitting $\psi_{ij} = \psi_0 + \hat{\psi} = -k\nabla\phi_0 - k\nabla\hat{\phi}$, where $\psi_0$ and $\hat{\psi}$ are characterised by

$$\nabla \cdot \psi_0 = 2 \text{ in } \Omega_1, \quad \phi_0 = 0, \quad \text{on } e_1, e_2, \tag{A.2}$$

$$\nabla \cdot \hat{\psi} = 0 \text{ in } \Omega_1, \quad \hat{\phi} = \phi_{ij}, \text{ on } e_1, e_2. \tag{A.3}$$

The problem (A.2) is symmetric about the line $x + y - 1 = 0$, so $f_h(\psi_0) = \int_{e2} \psi_0 \cdot \nu_2$, where $\nu_2$ is the outward-pointing unit normal to $e_2$. For $\hat{\psi}$, however, the corresponding flux integrals will have opposite signs, i.e., $f_h(\hat{\psi}) = -\int_{e2} \hat{\psi} \cdot \nu_2 \geq 0$, where the last inequality follows since $\hat{\phi}$ is nonnegative on $e_2$ and equals zero on $e_1$ (By the maximum principle, $\hat{\phi}_{ij}$ has minimal value 0, and thus $f_h(\hat{\psi}) \geq 0$). It now follows that $f_h(\psi_{ij}) \geq \int_{e2} \psi_{ij} \cdot \nu_2$, and that

$$f_h(\psi_{ij}) \geq \frac{1}{2} \int_{\Omega_1} \nabla \cdot \psi_{ij} \, dx = \frac{1}{2} \int_{\Omega_1} w_i \, dx = \frac{1}{4}.$$

This implies that $f_l(\psi_{ij}) = \int_{T_i} w_i - f_h(\psi_{ij}) \leq \frac{3}{4}$, and therefore $f_l^h(\psi_{ij}) \geq \frac{1}{3}$. From a similar argument for the lower left square $\Omega_3$, it follows that $f_l^h(\psi_{ij}) \leq 3$.

REFERENCES


[1] J. E. Aarnes, *On the use of a mixed multiscale finite element method for greater flexibility and increased speed or improved accuracy in reservoir simulation*, Multiscale Model. Simul. **2** (2004), no. 3, 421–439.

[2] J. E. Aarnes, V. Kippe, and K.-A. Lie, *Mixed multiscale finite elements and streamline methods for reservoir simulation of large geomodels*, Adv. Water Resorces. **28** (2005), no. 3, 257–271.

[3] J.E. Aarnes and K.-A. Lie, *Toward reservoir simulation on geological grid models*, Proceedings of the 9th European Conference on the Mathematics of Oil Recovery, EAGE, Cannes, France, 2004.

[4] T. Arbogast, *Numerical subgrid upscaling of two-phase flow in porous media*, Lecture Notes in Phys. (Z. Chen, R. Ewing, and Z.-C. Shi, eds.), Springer-Verlag, Berlin, 2000, pp. 35–49.

[5] ———, *Analysis of a two-scale, locally conservative subgrid upscaling for elliptic problems*, SIAM J. Numer. Anal. **42** (2004), no. 2, 576–598.

[6] T. Arbogast and K. Boyd, *Subgrid upscaling and mixed multiscale finite elements*, Submitted.

[7] T. Arbogast, S. E. Minkoff, and P. T. Keenan, *An operator-based approach to upscaling the pressure equation*, Computational Methods in Water Resources XII, Vol. 1: Computational Methods in Contamination and Remediation of Water Resources (Burganos et al., ed.), Computational Mechanics Publications, 1998, pp. 405–412.

[8] J.W. Barker and S. Thibeau, *A critical review of the use of pseudorelative permeabilities for upscaling*, SPE Reservoir Eng. (1997), no. 12, 138–143.

[9] A. Benesoussan, J.-L. Lions, and G. Papanicolaou, *Asymptotic analysis for periodic structures*, Elsevier Science Publishers, Amsterdam, 1978.

[10] Z. Chen and T. Y. Hou, *A mixed multiscale finite element method for elliptic problems with oscillating coefficients*, Math. Comp. **72** (2003), 541–576.

[11] M. A. Christie and M. J. Blunt, *Tenth SPE comparative solution project: A comparison of upscaling techniques*, SPE Reservoir Engineering and Evaluation **4** (2001), no. 4, 308–317, url: www.spe.org/csp.

[12] M.A. Christie, *Upscaling for reservoir simulation*, JPT J. Pet. Tech. (1996), no. 48, 1004–1010.

[13] L.J. Durlofsky, R.C. Jones, and W.J. Milliken, *A nonuniform coarsening approach for the scale-up of displacement processes in heterogeneous porous media*, Adv. Water Res. **20** (1997), 335–347.

[14] Y. Efendiev, V. Ginting, T. Hou, and R. Ewing, *Accurate multiscale finite element methods for two-phase flow simulations*, Submitted to J. Comput. Phys.

[15] B. Engquist and W. E, *The heterogeneous multiscale methods*, Comm. Math. Sci. **1** (2003), no. 1, 87–133.

[16] ———, *Multiscale modeling and computation*, Notices of the AMS **50** (2003), no. 9, 1062–1070.

[17] U. Hornung, *Homogenization and porous media*, Springer–Verlag, New York, 1997.

[18] T. Y. Hou and X.-H. Wu, *A multiscale finite element method for elliptic problems in composite materials and porous media*, J. Comput. Phys. **134** (1997), 169–189.

[19] T.J.R. Hughes, G.R. Feijoo, L. Mazzei, and J.-B. Quincy, *The variational multiscale method – a paradigm for computational mechanics*, Comput. Methods. Appl. Mech. Engrg. (1998), no. 166, 3–24.

[20] P. Jenny, S. H. Lee, and H. A. Tchelepi, *Multi-scale finite-volume method for elliptic problems in subsurface flow simulation*, J. Comput. Phys. **187** (2003), 47–67.

[21] ———, *Adaptive multiscale finite-volume method for multiphase flow transport in porous media*, Multiscale Model. Simul. **3** (2004), no. 1, 50–64.

[22] V.V. Jikov, S.M. Kozlov, and O.A. Oleinik, *Homogenization of differential operators and integral functionals*, Springer–Verlag, New York, 1994.

[23] Y. Kuznetsov, K. Lipnikov, and M. Shashkov, *The mimetic finite difference method on polygonal meshes for diffusion-type problems*, Comput. Geosciences **4** (2004), no. 8, 301–324.

[24] Y. Kuznetsov and S. Repin, *New mixed finite element method on polygonal and polyhedral meshes*, Russ. J. Numer. Anal. Math. Modellling **18** (2003), no. 3, 261–278.

[25] A.-M. Matache and C. Schwab, *Homogenization via p-fem for problems with microstructure*, Proceedings of the Fourth International Conference on Spectral and High Order Methods (ICOSAHOM 1998), vol. 33, 2000, pp. 43–59.

[26] P. Renard and G. de Marsily, *Calculating equivalent permeability*, Adv. Water Res. **20** (1997), 253–278.

[27] X.-H. Wen and J.J. Gómez-Hernández, *Upscaling hydraulic conductivities in heterogeneous media: An overview*, J. Hydrol. (1996), no. 183, ix–xxxii.